The Ulleung eddy owes its existence to β and nonlinearities

Wilton Z. Arruda [a,1], Doron Nof [a,*,2], James J. O'Brien [b]

[a] *Department of Oceanography 4320, The Florida State University, Tallahassee, FL 32306-4320, USA*

[b] *Center for Ocean Atmospheric Prediction Studies (COAPS), The Florida State University, Tallahassee, FL 32306-2840, USA*

Abstract

A nonlinear theory for the generation of the Ulleung Warm Eddy (UWE) is proposed. Using the nonlinear reduced gravity (shallow water) equations, it is shown analytically that the eddy is established in order to balance the northward momentum flux exerted by the separating western boundary current. In this scenario the presence of β produces a southward (eddy) force balancing the northward momentum flux imparted by the separating East Korean Warm Current.

The solution is derived using an expansion in powers of $\epsilon^{1/6}$ (here $\epsilon = \beta R_d/f_0$ where R_d is the Rossby radius based on the undisturbed upper layer thickness H). It is found that, for a high Rossby number western boundary current (i.e., highly nonlinear current) the eddy radius is roughly $2R_d/\epsilon^{1/6}$ implying that the UWE has a scale larger than that of most eddies (R_d). This solution shows that, in contrast to the familiar idea attributing the formation of eddies to instabilities (i.e., the breakdown of a known *steady* solution), the UWE is an integral part of the *steady* stable solution.

A reduced gravity numerical model is used to further analyze the relationship between β, nonlinearity and the eddy formation. First, we show that high Rossby number western boundary current which is forced to separate from the wall on an f-plane does not produce an eddy near the separation. To balance the northward momentum force imparted by the nonlinear boundary current the f-plane system moves offshore producing a southward Coriolis force. We then show that as, β is introduced to the problem, an anticyclonic eddy is formed. The numerical balance of forces shows that, as suggested by the analytical reasoning, the southward force produced by the eddy balances the northward force imparted by the boundary current. We also found that the observed eddy scale in the Japan/East Sea agrees with the analytical and numerical estimate for a nonlinear current.

Key words: Japan/East Sea, Ulleung Warm eddy, intrusion eddy, East Korea Warm Current, Western Boundary Currents

1 Introduction

The Japan/East Sea (JES) is a part of a chain of marginal seas adjacent to the northwestern Pacific. It is a deep semi-enclosed sea bounded by the Japanese Islands, the Korean Peninsula, and the Asian continent. With dimensions of about 1600 $\times$ 900 km and a maximum depth about 3700 m, it contains large-scale circulation features resembling those in major ocean basins (e.g., cyclonic and anticyclonic gyre systems and deep homogeneous water mass). The JES also contains wind-driven and thermohaline-driven circulation, deep convection, ice-sea interactions, and mesoscale circulation features. Here, we focus on one of the most prominent features of the JES, the Ulleung Warm Eddy (UWE).

1.1 Observational background

The northward flowing Tsushima Warm Current (TWC) has a major impact on the hydrography and circulation in the JES. Its minimum transport is in the summer-autumn, with an annual mean of 2 Sv and a seasonal variation of about 1.3 Sv (peak to peak) [Preller and Hogan, 1998]. Perkins et al. (2000) and Jacobs et al. (2001) verified the earlier ideas that, within the Tsushima Strait, the TWC is divided into two different currents, one flowing through the eastern channel and the other through the western channel. This so-called "primary branching" (Fig. 1) is thought to be due to the Tsushima Island and the topography but Ou (2001) proposed an alternative splitting mechanism. According to the classical interpretation of Suda and Hidaka (1932) and Uda (1934), the northern part of the TWC ultimately splits again forming a total of three distinct branches (Fig. 1) originally named (from east to west) first, second and third branches. The structure and variability of the TWC were studied using a variety of data sets: hydrographic (Kawabe, 1982a; Lie, 1984; Lie and Byun, 1985; Kim and Kim, 1983; Katoh, 1994; Preller and Hogan, 1998), satellite-derived sea-surface temperature (SST) (Kim and Legeckis, 1986; Cho and Kim, 1996), and numerical models experiments (Kawabe, 1982b; Hogan and Hurlburt, 2000).

For clarity we shall refer to the East Korean Warm Current (EKWC) as the

* Corresponding author.
Email addresses: arruda@coaps.fsu.edu (Wilton Z. Arruda), nof@ocean.fsu.edu (Doron Nof), obrien@coaps.fsu.edu (James J. O'Brien).
[1] Permanent address: Instituto de Matemática, Universidade Federal do Rio de Janeiro, Caixa Postal 68530, Rio de Janeiro, RJ 21945-970, BRAZIL
[2] Additional affiliation: Geophysical Fluid Dynamics Institute, The Florida State University, Tallahassee, Florida

"third branch" of the TWC. The EKWC flows northward along the continental slope off the east coast of Korea up to about 37-38°N, where it meets the much weaker southward-flowing North Korea Cold Current (NKCC) (Suda and Hidaka, 1932; Kim and Kim, 1983; Kim and Legeckis, 1986). At the confluence, the currents separate from the coast and flows east-northeast toward the Tsugaru Strait. This separation appears to be analogous to the classical western boundary current separation which occurs around 37-38°N (e.g. Gulf Stream), but it is probably forced by the Tsugaru strait outflow situated to the east.

Using ADCP (Acoustic Doppler Current Profiler) data, Katoh (1994) estimated that the transport of the EKWC amounted to about 1.54 Sv in June 1998, 0.70 Sv in August 1998, and 1.77 in June 1989. Tanioka (1968) argues that 80-90% of the volume transport of the EKWC returns southward around Ulleung Island forming the Ulleung Warm Eddy (UWE) (Ichiye and Takano, 1988; Kang and Kang, 1990; Kim et al., 1991; Katoh, 1994). The UWE is located in the central part of the Ulleung Basin (where the depth exceeds 1500 m) and has a diameter of approximately 150 km (Fig. 2).

Lim and Kim (1995) argued that topography is controlling the eddy's position, and Isoda and Saitoh (1993) reported the formation of a large-scale northward flow near the Korean coast when the eddy approaches the western slope of the continental margin. However, the eddy does not always migrate. Using satellite-tracked drifters, Lie et al. (1995) showed that the eddy was almost stationary from December 1992 to September 1993. They also suggested that the EKWC splits further into two parts: the main stream, which meanders around Ulleung Island, and a branch flowing northeast along the Korean coast. Besides the UWE, the JES shows a high eddy activity and various studies examined the horizontal eddy scales in the basin (Toba et al., 1982; Kim and Legeckis, 1986; Ichiye and Takano, 1988; Tameishi, 1987; Isoda and Nishihara, 1992; Sugimoto and Tameishi, 1992; Matsuyama et al., 1990; Miyao, 1994).

1.2 The EKWC separation

Our aim is to provide an explanation for the establishment of the UWE. To do so we shall assume that the EKWC leaves the coast due to a vanishing thermocline depth induced by the Tsugaru outflow to the East. There have been numerous studies of western boundary current separation and the reader is referred to: Parsons (1969), Veronis (1973), Huang and Flierl (1987), and Dengg et al. (1996). Two related aspects need to be addressed here. First, we shall examine the issue of whether the momentum flux of the opposing NKCC is negligible and, second, we shall show that the outflow through the Tsugaru strait in the eastern JES is most likely the cause of the separation.

1.2.1 The EKWC and NKCC momentum fluxes

We shall neglect the momentum flux of the NKCC on the ground that it is small in most of the time when compared with the momentum flux of the EKWC. To see this we note that the momentum flux of each boundary current can be approximated as

$$\int_0^\infty hv^2\,dx \simeq \bar{v}\int_0^\infty hv\,dx\ , \tag{1}$$

where $\bar{v}$ and $\int_0^\infty hv\,dx$ are the average speed and the transport over the boundary current respectively. Observations (Gordon, 1990; Preller and Hogan, 1998; Rostov et al., 2001) suggest that on average, the EKWC has a transport of ~ 1.5 Sv and a speed of ~ 25 cm s^{-1} while the NKCC has a transport of ~ 0.5 Sv and a speed ~ 5 cm s^{-1}. This gives a momentum flux ratio of 1/15 indicating that the momentum flux of the NKCC is usually negligible. Note, however, that these values change on various time spans and that, consequently, the momentum flux of NKCC is not always negligible. Using ADCP data collected during June-July 1999, Ramp et at. (2002) computed a transport of 1.45 Sv and a momentum flux of 2.27×10^5 m^4 s^{-2} for the EKWC and a transport of 0.78 Sv and a momentum flux of 1.59×10^5 m^4 s^{-2} for the NKCC. This gives a ratio of 0.7 for the momentum fluxes which is clearly not negligible. It is important to realize that, for the time period considered by Ramp et at. (2002) no UWE was observed. Consequently, they could apply the theory for the collision of boundary currents on an f-plane (Agra and Nof, 1992) and conclude that the separated current should leave the coast at a calculated angle of 80° which was in very good agreement with their observations.

1.2.2 The mechanism forcing the EKWC separation

To see that, for most of the year, the wind stress (which is the classical force associated with separation) may not play an important role in the EKWC separation, consider the depth integrated linear reduced gravity x-momentum equation,

$$-fV = -\frac{g'}{2}\frac{\partial(h^2)}{\partial x} + \frac{\tau^x}{\rho}\ , \tag{2}$$

where h is the upper layer thickness, V is the vertically integrated velocity component in the y direction, g' the reduced gravity, τ^x the zonal wind stress component (assumed to be a function of y only) and ρ is the upper layer density. Integrating (2) zonally across the basin and temporality assuming that there is no net meridional volume transport through the section (i.e., no "sink"), we have

$$h_{eb}^2 - h_{wb}^2 = \frac{2\tau^x}{\rho g'}\, L_e \,,$$

where h_{wb} and h_{eb} are the wind induced upper layer thicknesses on the western boundary and eastern boundary respectively, and L_e is the basin length. At the separation latitude $h_{wb} = 0$, so

$$h_{eb} = \left(\frac{2\tau^x}{\rho g'}\, L_e\right)^{1/2} . \tag{3}$$

Using (3) and the climatological Hellerman-Rosenstein zonal wind stress for 37° N, we can calculate monthly values for the no-sink wind-induced upper layer thickness h_{eb}. From November to March the average zonal wind stress is high (0.78 dyn cm^{-2} for January) giving a mean value of 57 m for h_{eb}. For the rest of the year the average zonal wind stress is much weaker (giving h_{eb} of 10 m for April) and even negative from May to October. According to Chu et al. (2001), the the upper layer thickness on the eastern boundary is between 150 and 200 m from November to April, indicating that, even during the strong wind stress period, the calculated h_{eb} is too small. We conclude that the JES has a too short zonal width to accommodate a separation of the EKWC by the wind stress, indicating that the Tsugaru strait outflow is the main mechanism responsible for the EKWC separation.

1.3 Objectives of the present study

Observations off the East Australia Current and numerical simulations of the Brazil Current (Olson, 1991) suggest that the separation mechanism of a western boundary current leads to the formation of an "intrusion eddy" [3] . In what follows we shall argue that the UWE belongs to the same category. The identification of physical mechanism responsible for the existence of the intrusion eddy is the focus of this paper.

This paper is organized as follows: In section 2 we derive an analytical relationship that represents the balance of forces in a control region surrounding the eddy. In section 3 we derive an estimate for the eddy radius based on the relation found in section 2. In section 4 we describe the comparison between the analytical results from the previous sections and the outputs of a numerical model. In section 5 we investigate the linear limit and in section 6 we discuss the results and present the conclusions.

[3] This term was first used by Olson (1991) to describe an eddy associated with a western boundary current separation.

2 Formulation

We shall study the "intrusion eddy" (formed when a western boundary current separates from the coast due to an outflow east of the boundary) in the framework of a baroclinic reduced gravity model on a β-plane (Fig. 3). Though the wind stress and the ocean interior are responsible for the existence of the western boundary current in the ocean, we assume that their role in the dynamics of the eddy is minor, because the length scale of the wind systems is much greater than that of the boundary current [$\sim O(R_d)$].

Consider a single northward flowing western boundary current in an upper layer (with density ρ) above an infinitely deep layer of slightly denser water (with density $\rho + \Delta\rho$). As the current flows northward it reaches a latitude where the upper layer thickness vanishes on the wall due to the outflow to the east and, consequently, a separation takes place. We place the origin of our coordinate system right on separation point on the wall and assume that far away from the western boundary and far south from the separation latitude the upper layer thickness approaches an undisturbed value H. As alluded to earlier the effects of an opposing southward flowing boundary current are neglected.

The separated current forms a front where the outcropping streamline divides the domain into two sections. Both layers are present in the southern part of the basin but only one (the motionless denser layer) is present in the northern part. As we shall see later, it will not be necessary for us to derive the solution for the entire region and the separation point because we shall use an integrated approach which that avoids need. A schematic diagram of our domain of study is depicted in Fig. 4.

2.1 North-South momentum balance

Assuming a steady state and integrating (after multiplying by h) the steady and inviscid nonlinear y-momentum equation,

$$u\frac{\partial v}{\partial x} + v\frac{\partial v}{\partial y} + fu + g'\frac{\partial h}{\partial y} = 0,$$

over the fixed region S bounded by the dashed line $ABCDA$ shown in Fig. 4, we get

$$\iint\limits_S (hu\frac{\partial v}{\partial x} + hv\frac{\partial v}{\partial y})\, dx\, dy + \iint\limits_S (f_0 + \beta y)uh\, dx\, dy$$

$$+\frac{g'}{2}\iint\limits_S \frac{\partial(h^2)}{\partial y}\,dx\,dy = 0, \tag{4}$$

which, by using the continuity equation and stream function ψ, can be reduced to

$$\iint\limits_S \left[\frac{\partial(huv)}{\partial x} + \frac{\partial(hv^2)}{\partial y}\right] dx\,dy - \iint\limits_S (f_0 + \beta y)\frac{\partial\psi}{\partial y}\,dx\,dy$$
$$+\frac{g'}{2}\iint\limits_S \frac{\partial(h^2)}{\partial y}\,dx\,dy = 0. \tag{5}$$

Here, the notation is conventional, that is, u and v are the velocity components in the x and the y direction, h is the upper layer thickness, ψ is the transport stream function defined by $\partial\psi/\partial y = -uh$; $\partial\psi/\partial x = vh$, and g' is the reduced gravity, $g\Delta\rho/\rho$ (for convenience variables are defined both in the text and in Appendix).

Eq. (5) can be rewritten as,

$$\iint\limits_S \left[\frac{\partial(huv)}{\partial x} + \frac{\partial(hv^2)}{\partial y}\right] dx\,dy - \iint\limits_S f_0\frac{\partial\psi}{\partial y}\,dx\,dy$$
$$-\iint\limits_S \left[\frac{\partial(\beta y\psi)}{\partial y} - \beta\psi\right] dx\,dy + \frac{g'}{2}\iint\limits_S \frac{\partial(h^2)}{\partial y}\,dx\,dy = 0\,, \tag{6}$$

and application of Green's theorem gives

$$\oint\limits_{\partial S} huv\,dy - \oint\limits_{\partial S}\left(hv^2 + \frac{g'h^2}{2}\right) dx + f_0\oint\limits_{\partial S}\psi\,dx$$
$$+\beta\oint\limits_{\partial S} y\psi\,dx + \beta\iint\limits_S \psi\,dx\,dy = 0, \tag{7}$$

where ∂S is the boundary of S.

Next, we assume that $\psi = 0$ along the wall and on the outcropping front and note that at least one of the three variables h, u, and v vanishes on every portion of the boundary ∂S. It then follows from (7) that

$$\int\limits_A^B \left[hv^2 + \frac{g'h^2}{2} - (f_0 + \beta y)\psi\right] dx - \beta\iint\limits_S \psi\,dx\,dy = 0. \tag{8}$$

Assuming now that the flow is geostrophic in the cross-current direction, we get [after multiplying the geostrophic relation $(f_0+\beta y)v = g'\partial h/\partial x$ by h and integrating on the segment AB],

$$(f_0+\beta y)\psi + C = \frac{g'}{2}h^2, \tag{9}$$

where C is the constant to be determined. Note that at $x\to\infty$ the the zonal flow is geostrophic in the y direction so that

$$(f_0+\beta y)uh = -\frac{g'}{2}\frac{\partial(h^2)}{\partial y}\,,$$

and an integration in y gives,

$$(f_0+\beta y)\psi\Big|_{y_s}^{y_n} - \beta\int_{y_s}^{y_n}\psi_\infty\,dy = \frac{g'}{2}h^2\Big|_{y_s}^{y_n},\quad x\to\infty$$

where ψ_∞ (which is a function of y) is the stream function at $x\to\infty$, and y_s and y_n are the y-components of points A and D (Fig. 4) respectively. Since $\psi = h = 0$ at $y = y_n$ it follows that $C = \beta\int_{y_s}^{y_n}\psi_\infty\,dy$ so that (8) can be written as,

$$\int_0^L hv^2\,dx - \beta\iint_S(\psi-\psi_\infty)\,dx\,dy = 0, \tag{10}$$

where L is the width of the boundary current. Note that the integrand of the second integral vanishes as $x\to\infty$ and, consequently, the integral does not change when the zonal extent of S is increased (as should be the case).

Let y_0 be the latitude where $\psi_\infty = 0$. Then, from (9)

$$\int_0^L hv^2\,dx - \beta\iint_{S^+}\psi\,dx\,dy - \beta\iint_{S^-}(\psi-\psi_\infty)\,dx\,dy = 0, \tag{11}$$

where S^+ and S^- are subsets of S corresponding to $y > y_0$ and $y \le y_0$, respectively.

We shall now leave (11) temporarily aside and discuss the relevant scales.

2.2 Scaling

Assuming nonlinear dynamics we take the following scales:

$$L \sim O(R_d); \;\; v \sim O\left((g'H)^{1/2}\right);$$
$$\psi \sim O\left(\frac{g'H^2}{f_0^2}\right) \text{outside the eddy}; \;\; \psi \sim O\left(\frac{g'H_e^2}{f_0^2}\right) \text{inside the eddy},$$

where $R_d = (g'H)^{1/2}/f_0$ is the Rossby radius of deformation, and $H_e \gg H$ is the depth scale for the eddy.

Note that the integrand of the third term in (11) is zero in the area outside the currents so each term of (11) can be scaled as,

$$\int_0^L hv^2\,dx \sim O\left(g'H^2R_d\right) \tag{12}$$

$$\beta \iint_{S^-} (\psi - \psi_\infty)\,dx\,dy \sim O\left(\beta R_d L_2 \frac{g'H^2}{f_0}\right) \tag{13}$$

$$\beta \iint_{S^+} \psi\,dx\,dy \sim O\left(\beta R_{de}^2 \frac{g'H_e^2}{f_0}\right), \tag{14}$$

where $R_{de} = (g'H_e)^{1/2}/f_0$, $|y_s| = L_2 \gg R_d$, and L_2 is the length of the integration domain $ABCD$ (Fig. 4). Note that the ratio between (13) and (12) is $\beta L_2/f_0 \ll 1$. Consequently, the only term that can balance the momentum flux (12) is the β term (14). Taking

$$R_{de} \sim O\left(\frac{Rd}{\epsilon^{1/6}}\right), \text{ and} \tag{15}$$

$$L_2 \sim O(R_{de}), \tag{16}$$

where $\epsilon = \beta R_d/f_0 \ll 1$, we have a balance between (12) and (14) and the ratio between (12) and the two other terms is $O(\epsilon^{5/6})$.

Two comments should be made with regard to (14). First, as is frequently the case, the scaling may conceal potentially large numbers such as powers of the known $2\sqrt{2}$ ratio between the eddy radius and the Rossby radius (see, e.g. Nof, 1981; Killworth, 1983). Second, the 1/6 power of ϵ implies that, for most cases [$\epsilon \sim O(0.1)$], R_{de} will comparable to R_d (though it will be somewhat larger).

2.3 Solution

The scale analysis performed in the last section shows that the leading order nonlinear balance is,

$$\int_0^L hv^2\, dx = \beta \iint_{S^+} \psi\, dx\, dy\ . \tag{17}$$

To find an estimate for the eddy radius, we shall first look at the case where both the eddy and the western boundary current have zero potential vorticity, i.e., the highly nonlinear case. Note that this zero potential vorticity limit makes the solutions for the boundary current and the eddy straightforward despite the nonlinearity. We shall see later that, for this limit, we obtain a lower bound estimate for the eddy radius.

2.3.1 Zero potential vorticity boundary current

For a zero-pv northward flowing boundary current,

$$v = \begin{cases} f(L-x)\ , & x \le L \\ 0 \qquad\qquad , & x > L \end{cases} \tag{18}$$

$$h = \begin{cases} H - \dfrac{f^2(L-x)^2}{2g'}\ , & x \le L \\ H \qquad\qquad\qquad , & x > L\ , \end{cases} \tag{19}$$

where, as mentioned, L is the width of the current.
From (19) it follows that along the wall ($x = 0$),

$$h(0, y) = H - \frac{f^2L^2}{2g'},\ \ y < 0. \tag{20}$$

Since the transport of the geostrophic boundary current through the zonal segment AB (Fig. 4) must be the same as the transport of the separated geostrophic current through the meridional segment BC (Fig. 4), we have

$$\frac{g'}{2f}\left(H^2 - h^2(0, y_s)\right) = \frac{g'}{2f_0}\, H^2\ ,$$

implying that

$$h(0,y) = H\left(\frac{\beta|y|}{f_0}\right)^{1/2}, \quad y < 0 \,. \tag{21}$$

Combining (20) and (21), we get an expression for the upstream boundary current width L,

$$L = \frac{(2g'H)^{1/2}}{f}\left[1 - \left(\frac{\beta|y|}{f_0}\right)^{1/2}\right]^{1/2} .$$

Note that the upper layer thickness h in (21) vanishes at $y = 0$ so that the separation condition is satisfied. The actual separation latitude is a Rossby radius upstream from $y = 0$, because the geostrophic assumption is not valid in the vicinity of the separation point.

Since $|y_s| \sim O(R_{de})$, if follows that $\beta|y_s|/f_0 \sim O(\epsilon^{5/6})$, implying that to leading order,

$$L = 2^{1/2} R_d \,. \tag{22}$$

By combining (18), (19), and (22), we find that the momentum flux imparted on the region S by the upstream boundary current through the zonal segment AB (Fig. 4) is to leading order,

$$\int_0^L hv^2 \, dx = \frac{1}{15}\, 2^{5/2} f_0^2 H R_d^3 \,. \tag{23}$$

This relationship will be employed shortly.

2.3.2 Zero potential vorticity eddy

The right hand side of (17) includes contributions from both the eddy and the separated current surrounding it. It is easy to see that the second contribution can be scaled as $O(\beta R_d R_{d_e} g' H^2/f_0)$ and that its ratio to $\beta \iint_{eddy} \psi \, dx \, dy$, is of $O(\epsilon^{5/6})$. So, to find an estimate for the β term we can take $\psi = \psi_e$, where ψ_e is the zero potential eddy stream function.

For a zero-pv eddy,

$$v_\theta = -\frac{f_0 r}{2}, \quad r \leq R_1 \tag{24}$$

$$h_e = H_e\left(1 - \frac{r^2}{R_1^2}\right), \quad r \leq R_1 \ , \tag{25}$$

where, v_θ is the orbital speed, r is the radial distance from the center of the eddy, h_e is the eddy upper layer thickness, H_e is the maximum thickness, and $R_1 = (8g'H_e)^{1/2}/f_0$. It follows from (25) that the eddy radius is,

$$R = \left[\frac{8g'(H_e - H_b)}{f_0^2}\right]^{1/2} , \tag{26}$$

where H_b is the depth on the closed stream line bounding the eddy. The corresponding stream function for the eddy is,

$$\psi_e = \frac{f_0^3}{2^6 g'}(R_1^2 - r^2)^2 + K \ ,$$

where the constant K is found by matching the transport of the separated boundary current with the value of the stream function along the eddy boundary ($\psi_e = g'H_b^2/2f_0$ at $r = R$). This gives $K = -g'H_b^2/2f_0$ so that,

$$\psi_e = \frac{f_0^3}{2^6 g'}(R_1^2 - r^2)^2 - \frac{g'H_b^2}{2f_0}, \quad y \leq R \ . \tag{27}$$

It is worth pointing out here that it is obvious that this solution conserves the potential vorticity along the streamlines but it is less obvious that it conserves the Bernoulli function. It is easy to see, however, that the Bernoulli is also conserved because the eddy's streamlines are closed so that the Bernoulli function inside the eddy ($g'H_e$) need not be equal to that outside the eddy ($g'H$).

As a consequence of (15), we have $H_e \sim O(\epsilon^{-2/6}H)$, and in view of (26) and (27) it follows that to the leading order,

$$R = R_1 \ \text{ and } \ \psi_e = \frac{f_0^3}{2^6 g'}(R^2 - r^2)^2 \ , \ r \leq R \ . \tag{28}$$

Then, integrating (28) over the eddy we get,

$$\iint_{eddy} \psi_e \, dx \, dy = 2^{-6}\left(\frac{\pi}{3}\right)\frac{f_0^3}{g'^2} R^6 \ , \tag{29}$$

which just like (23) will be shortly used to get our solution.

2.3.3 Final solution

By combining (17), (23), and (29), we obtain our desired nonlinear eddy scale

$$\boxed{R = 2\left(\frac{2^{5/2}}{5\pi}\right)^{1/6}\frac{R_d}{\epsilon^{1/6}}}\,. \tag{30}$$

Relation (30) is an analytical estimate for the eddy radius based on our momentum balance approach. It relates the eddy size to the known physical parameters upstream. It is opportune to point out that (30) is a lower bound estimate for the eddy radius, because the zero pv eddy is highly nonlinear and, as a consequence, it is the steepest anticyclonic eddy possible.

3 Numerical simulations

In order to test our analytical result and further investigate the role of β in the eddy formation, numerical simulations are performed and the results are quantitatively analyzed. In these simulations we compare the evolution of the system on both f-plane and β-plane (for the same set of physical parameters).

3.1 Numerical Model Description

We use a reduced gravity version of the isopycnic model developed by Bleck and Boudra (1981,1986) and later improved by Bleck and Smith (1990). This model is suitable for our study since it allows isopycnic outcropping by using the "Flux-Corrected Transport" algorithm (Boris and Book, 1973; Zalesak, 1979) in the continuity equation.

The equations of motion are the two momentum equations,

$$\begin{aligned}
\frac{\partial u}{\partial t} + u\frac{\partial u}{\partial x} + v\frac{\partial u}{\partial y} - (f_0 + \beta y)v &= -g'\frac{\partial h}{\partial x} + \frac{\nu}{h}\nabla\cdot(h\nabla u)\\
\frac{\partial v}{\partial t} + u\frac{\partial v}{\partial x} + v\frac{\partial v}{\partial y} + (f_0 + \beta y)u &= -g'\frac{\partial h}{\partial y} + \frac{\nu}{h}\nabla\cdot(h\nabla v)\ ,
\end{aligned}$$

and the continuity equation

$$\frac{\partial h}{\partial t} + \frac{\partial (hu)}{\partial x} + \frac{\partial (hv)}{\partial y} = 0,$$

where ν is the friction coefficient.

The model uses the Arakawa (1966) C-grid where the u-velocity points are shifted one-half grid step to the left from h points, the v-velocity points are shifted one-half grid step down from the h points, and vorticity points are shifted one-half grid step down from the u-velocity points. The integration domain is rectangle with a closed western and northern boundaries, open eastern boundary, and imposed inflow on the southern boundary. The Orlanski (1976) second-order radiation boundary condition was implemented on the open boundary .

Three extensive experiments were performed and the respective parameters are listed in Table 1. Additional experiments are not necessary for two reasons. First, the parameter controlling the experiment is the undisturbed upper layer thickness H as it sets up both the the boundary current transport $(g'H/2f_0)$ and the Rossby radius of deformation R_d. So, all boundary current parameters are determined by H, and consequently, after nondimensionalizing the equations of motion of any two runs would differ only by the nondimensional β $(\beta R_d/f_0)$ and the nondimensional coefficient of friction $(\nu/f_0R_d^2)$. As long as the western boundary current is inertial the parameter $\beta R_d/f_0$ is the only one that is controlling the experiment. In midlatitude the parameter $\beta R_d/f_0$ does not have a significant variation so three experiments are sufficient. Second, for each of the three experiments that are conducted, we let the model run for 10,000 days, giving a massive data set.

The parameters adopted for the main experiment E1 are indicated in Table 1. The baroclinic Rossby radius of deformation is 25 km and the transport of the boundary current is about 7.7 Sv (1 Sv = 10^6 m^3 s^{-1}). Due to computer time limitation we take a time step of 720 seconds and a grid size of 15 km, so that we are barely resolving the Rossby radius. Since the eddy is greater than the Rossby radius this is not an issue. It would, of course, been better to use a higher resolution but, as we shall see, the results are so robust that this apparent weakness is not significant. We adopt the free slip boundary condition and a relatively large horizontal friction ($\nu = 1500$ m^2 s^{-1}) in order to smooth out transient features. The initial condition for the β-plane experiments is the day 200 fields of an f-plane run with a zonal wall dividing the domain (the f-plane experiment will be discussed later). On the southern edge we use the same parameters as above and on the northern edge the upper layer thickness is zero. We then take the wall out and, at the same time turn beta on. We then let the system evolve for 10,000 days.

For economical reasons the parameters used in the numerical experiment E1 are not identical to those of the JES, where the EKWC has transport of merely 1.5 Sv (which would imply an undisturbed upper layer thickness H = 133 m). For the real JES the Rossby radius of deformation would be smaller and we would have to decrease the integration time step, making our runs more time consuming. This is not an issue even though our β effect is stronger than that in the JES, because it merely makes our runs spin up faster.

3.2 General results

Fig. 5 and Fig. 7b,d show the contour plots of the nondimensional upper layer thickness for the f-plane run (experiment E3 in Table 1) at days 100, 500, 1000, and 3000. The most important aspect is that there is no eddy. Even though there is an area of increased upper layer thickness and transport due to accumulation of fluid displaced from the western boundary, the resulting circulation is much weaker than that of the β-plane run (Fig. 7a,c). It can be seen that the entire system moves offshore and, consequently, it cannot reach a steady state. In order to highlight the offshore movement of the system we plot in Fig. 6, the 0.3 contour for each of the days depicted in Fig. 5. In analogy with the ballooning outflow situation studied by Nof and Pichevin (2001), the eastward movement of the separated boundary current produces a Coriolis force directed to the south. This force balances the northward momentum flux of the separated boundary current.

In Fig. 7, we plot side by side snapshots of the nondimensional upper layer thickness and nondimensional streamfunction at day 3000 for the β-plane experiment E1 and f-plane experiment E3 (Table 1). This day is chosen as a representative of the entire experiment E1 because it reflects a steady solution. We see that the intrusion eddy is a very prominent feature on the β-plane plots [Fig. 7a,d] with maximum nondimensional upper layer thickness greater than 1.3 and maximum nondimensional transport of 2. It is important to note that the boundary current is inertial (i.e., nonlinear) as its width is $O(R_d) = 25$ km, much smaller than the frictional boundary layer width $O\left[(\nu/\beta)^{1/3}\right] = 200$ km. Here, the friction used is high enough to avoid the transient features but not so large to change the dynamics of the boundary current. The downstream zonal flow is broad compared with the upstream boundary current due to friction diffusivity. To go further with the comparison of the numerical results to our analytical relations, let's rewrite (8), using (9) evaluated at $x = 0$ and assuming that $\psi = 0$ on the wall. Then

$$\underbrace{\int_0^L hv^2\, dx}_{\text{momentum flux}} \quad \underbrace{+\frac{g'}{2} h^2(0, y_s) L_2}_{\text{pressure}} \underbrace{- \beta \iint_S \psi\, dx\, dy}_{\beta\text{-force}} = 0, \tag{31}$$

where L is the boundary current width and L_2 is the length of the segment AB (see Fig. 4). In this form (31) represents a balance between three forces.

The first is the northward force associated with the momentum flux of the alongshore current. The second is a northward pressure force due to the difference in thickness on the wall between points A and D (Fig. 4). The third term is a southward β-force resulting from the fact that a particle circulating anticyclonically within the eddy senses a larger Coriolis force on the northern than it senses on the southern side of the path.

Fig. 8 displays each term of (31). It is evident that the intrusion eddy exists in order to balance the northward momentum flux of the western boundary current because, according to (17) and the scale analysis, the eddy is the major contributor for the net β term [combination of the second and third terms in (31)].

As stated before, the frictional coefficient used acts merely to smooth out transient features and does not play an important role in the integrated momentum balance. To verify that this is indeed the case, we performed experiment E2 (Table 1) with lower friction and we got essentially the same results as in E1. The only difference between the two is that here the separated current showed meanders that eventually closed upon themselves pinching off eddies that died off (or were reattached to the main flow after some time).

In Fig. 9 we show the analytical estimate of the eddy radius from (30) against the numerical estimate [taking the 1.3 closed (nondimensional) streamline as the eddy boundary (Fig. 5)]. As expected, the radius based on the zero potential vorticity assumption is a lower bound for the actual eddy radius because the zero pv eddy is the steepest possible eddy (Nof, 1981; Killworth, 1983). Nevertheless, the agreement is pretty good, as we get 4.2 R_d for the analytical estimate and about 5 R_d (after day 1000) for the numerical estimate.

4 The linear dynamics

We shall now show that for a small Rossby number flow (i.e., a linear geostrophic flow) there is no eddy associated with the current separation from the coast. In the linear limit, the boundary current width is large (due to the frictional nature of the boundary layer) compared with the Rossby radius so that the current is slower and the associated momentum flux is negligible. As we will see, in this situation the frictional dissipation balances the β term in the boundary layer and no eddy is necessary.

Consider the familiar, steady linear reduced-gravity (depth integrated) equations of motion for the upper layer

$$-fvh = -\frac{g'}{2}\frac{\partial(h^2)}{\partial x} + \frac{\tau^x}{\rho} \tag{32}$$

$$fuh = -\frac{g'}{2}\frac{\partial(h^2)}{\partial y} - \kappa vh \tag{33}$$

$$\frac{\partial(uh)}{\partial x} + \frac{\partial(vh)}{\partial y} = 0, \tag{34}$$

where κ is the interfacial friction coefficient and the rest of the notation was previously defined. In the inviscid interior, Sverdrup dynamics dominates the field. Within the western boundary current interfacial friction dissipates the energy input of the wind over the entire basin.

4.1 Momentum balance in the whole domain

Integrating the y-momentum equation (33) over the integration area S (containing the western boundary current) bounded by $ABCD$ (Fig. 10), and assuming that $\psi = 0$ on the bounds of the region containing the upper layer, we find,

$$\int_0^{x_B} \left[\frac{g'}{2}h^2 - (f_0 + \beta y)\psi\right] \, dx - \beta \iint_S \psi \, dx \, dy - \kappa \int_{y_s}^{y_n} \psi|_{x=L} \, dy = 0 \,, \tag{35}$$

where L is the boundary current width, $\psi|_{x=L}$ is the stream function at $x = L$, x_B is the x-component of B and y_s and y_n are the y-components of A and D respectively (Fig. 10). We shall now leave (35) aside for a moment and discuss the interior.

4.2 The interior balance

We note from (33) that in the inviscid ocean interior (where friction is unimportant),

$$\frac{\partial}{\partial y}\left[\frac{g'}{2}h^2 - (f_0 + \beta y)\psi\right] = -\beta\,\psi \,, \tag{36}$$

which can be integrated from y_s to y_n to give,

$$\left[\frac{g'}{2}h^2 - (f_0 + \beta y)\psi\right]_{y=y_s} = \beta \int_{y_s}^{y_n} \psi \, dy \tag{37}$$

for any $x > L$. Integrating (37) from $x = L$ to $x = x_B$, we get

$$\int_L^{x_B} \left[\frac{g'}{2} h^2 - (f_0 + \beta y)\psi \right] dx - \beta \int_L^{x_B} \int_{y_s}^{y_n} \psi \, dy \, dx = 0. \tag{38}$$

This balance is valid in the integration domain (S) within the ocean interior.

4.3 The western boundary layer balance

Subtracting (38) from (35) we obtain,

$$\int_0^L \left[\frac{g'}{2} h^2 - (f_0 + \beta y)\psi \right] dx - \beta \int_{y_s}^{y_n} \int_0^L \psi \, dx \, dy - \kappa \int_{y_s}^{y_n} \psi|_{x=L} \, dy = 0\,. \tag{39}$$

Neglecting the wind stress term (since its role is minor in the boundary current), it follows from (32) that

$$\frac{g'}{2} h^2 - (f_0 + \beta y)\psi = C \quad , x \leq L\,, \tag{40}$$

where C is a constant to be determined by matching (40) and (37) at $x = L$, obtaining $C = \int_{y_s}^{y_n} \psi|_{x=L} \, dy$. Substituting (40) into (39), we obtain

$$\beta \int_{y_s}^{y_n} \int_0^L (\psi - \psi|_{x=L}) \, dx \, dy + \kappa \int_{y_s}^{y_n} \psi|_{x=L} \, dy = 0. \tag{41}$$

The integrand of the second term of (41) is positive, implying that the first term should be negative. Note that an anticyclonic eddy would make a negative contribution to the β term. By scaling (41), it follows that the boundary current by itself produces a β-force that is able to balance the friction dissipation [second term in (41)] as long as $L \sim O(\kappa/\beta)$ (which is the well known Stommel boundary layer scale).

We see that (41) represents a balance between the β-force in the western boundary current and the frictional dissipation of the integrated wind stress curl over the entire basin. Under these conditions, no eddy is necessary for the required momentum balance showing that the establishment of the intrusion eddy is due to inertia (nonlinearities) and β.

5 Conclusions

Taking into account that the western boundary current in the JES is forced to separate from the coast by an outflow to the east, we derived a theory for the existence of the "intrusion eddy". Our analytical relations and numerical simulations show that, without the generation of the eddy, the nonlinear momentum flux of the northward flowing boundary current on a β-plane could not have been balanced [on an f-plane the situation is quite different. To balance the northward momentum force imparted by the boundary the system simply moves offshore (Fig. 6) producing a southward Coriolis force]. On this basis, we argue that the existence of the UWE is not related to instabilities but rather is due to β and nonlinearities (Fig. 7 and Fig. 8). Furthermore, we argue that the UWE semi-permanent characteristic is not due to topographic arrest but rather a part of the dynamics which includes the generation of a permanent eddy (Fig. 7a,c). For a mean transport of ~ 1.5 Sv for the EKWC, we find a Rossby radius of 16.3 km, and an $\epsilon^{1/6}$ of 0.39. Our predicted value for the UWE diameter from (30) is then 141 km, which agrees fairly well with the observed 150 km radius (Fig. 2) suggesting that its generation is related with the mechanism proposed here.

The present theory cannot be applied to the Gulf stream and Brazil-Malvinas confluence for three reasons. First, in both cases there are strong opposing (cold) currents (Labrador current in the first case and the Malvinas current in the second) whose momentum fluxes cannot be neglected. Second, there is a marked difference in density between the two colliding currents so that the denser (colder) current would slide under the less dense current and even separate form the coast in a different latitude. Third, there is a coastline tilt in both cases that could cause significant change in the momentum balance.

Acknowledgements. This study was supported by the Binational Science Foundation grant 96-105; National Science Foundation contract OCE 9911324; National Aeronautics and Space Administration grants NAG5-7630 and NAG5-10860; and Office of Naval Research grant N00014-01-0291. Wilton Z. Arruda was funded by Conselho Nacional de Desenvolvimento Científico e Tecnológico (CNPq-Brazil) under grant 202436/91-8 and fellowship from the Inter-American Institute for Global Change Research (IAI) through South Atlantic Climate Change Consortium (SACC). COAPS receives its base support from Secretary of Navy grant to James J. O'Brien. The authors would like to thank Dr. Nabuo Suginohara and Dr. Steven Ramp for their helpful comments and careful reading of the manuscript.

References

Agra, C., and D. Nof, 1993. Collision and separation of boundary currents. Deep-Sea Research I 40, 2259-2282.

Arakawa, A., 1966. Computational design for long-term numerical integration of the equations of fluid motion. Two dimensional incompressible flow. Part 1. Journal of Computational Physics 1, 1119-143.

Bleck, R., and D. Boudra, 1981. Initial test of a numerical ocean circulation model using a hybrid, quasi-isopycnic vertical coordinate. Journal of Physical Oceanography 11, 755-770.

Bleck, R., and D. Boudra, 1986. Wind-driven spin-up in eddy-resolving ocean models formulated in isopycnic and isobaric coordinates. Journal of Geophysical Research 91, 7611-7621.

Bleck, R., and L. Smith, 1990. A wind-driven isopycnic coordinate model of the north and equatorial Atlantic Ocean. Part I: Model development and supporting experiments. Journal of Geophysical Research 95, 3273-3285.

Boris, J., and D. Book, 1973. Flux-corrected transport, I: SHASTA, a fluid transport algorithm that works. Journal of Computational Physics 11, 38-69.

Cho, Y.-K., and K. Kim, 1996. Seasonal variation of the East Korea Warm Current and its relation with the cold water. La Mer 34, 172-182.

Chu, P. C., J. Lan, and C. W. Fan, 2001. Japan Sea circulation and thermohaline structure, Part 1, Climatology. Journal of Physical Oceanography 31, 244-271.

Dengg, J., A. Beckmann, and R. Gerdes, 1996. The Gulf Stream Separation Problem. In Warmwatersphere of North Atlantic Ocean, W. Krauss (ed.), Gebr. Bornträger, Sttutgard, pp. 253-290.

Gordon, A. L., 1990: Sea of Japan. In Marginal Seas and the Kuroshio: An Assessment of Mutual Impact, Department of Oceanography, Florida State University, Tallahassee, Fla.

Hogan, P. J., and H. Hurlburt, 2000. Impact of upper ocean-topographical coupling and isopycnal outcropping in Japan/East Sea models with 1/8° to 1/64° resolution. Journal of Physical Oceanography 30, 2535-2561.

Huang, R. X., and G. R. Flierl, 1987. Two-layer models for the thermocline and current structure in subtropical/subpolar gyres. Journal of Physical Oceanography 17, 872-884.

Ichiye, T., and K. Takano, 1988. Mesoscale eddies in the Sea of Japan. La Mer 26, 69-79.

Isoda, Y., and M. Nishihara, 1992. Behavior of warm eddies in the Japan Sea. Umi to Sora 67 (Spec. Issue), 231-243.

Isoda, Y., and S.-I. Saitoh, 1993. The northward intruding eddy along coast of Korea. Journal of Oceanography 49, 443-458.

Jacobs, G. A., H. T. Perkins, W. J. Teague and P. J. Hogan, 2001. Summer transport through the Tsushima-Korea Strait. Journal of Geophysical Research 106, 6917-6829.

Kang, H. E., and Y. Q. Kang, 1990. Spatio-temporal characteristics of the Ulleung Warm Lens. Bulletin of the Korean Fisheries Society 203, 407-415.

Katoh, O., 1994. Structure of the Tsushima Current in the southwestern Japan Sea. Journal of Oceanography 50, 317-338.

Kawabe, M., 1982a. Branching of Tsushima Current in the Japan Sea. Part I. Data Analysis. Journal of the Oceanographical Society of Japan 38, 95-107.

Kawabe, M., 1982b. Branching of Tsushima Current in the Japan Sea. Part II. Numerical experiment. Journal of the Oceanographical Society of Japan 38, 183-192.

Killworth, P. D., 1983. On the motion of isolated lenses on a beta-plane. Journal of Physical Oceanography 13, 368-376.

Kim, C. H., and K. Kim, 1983. Characteristics and origin of the cold water mass along the east coast of Korea. Journal of the Oceanological Society of Korea 18, 73-83.

Kim, K., and R. Legeckis, 1986. Branching of the Tsushima Current in 1981-83. Progress in Oceanography 17, 265-276.

Kim, K., K.-R. Kim, J. Chung, H. Yoo, and S. Park, 1991. Characteristics of physical properties in the Ulleung Basin. Journal of the Oceanological Society of Korea 26, 83-100.

Lie, H.-J., 1984. Coastal current and its variation along the east coast of Korea. In Ocean Hydrodynamics of the Japan and East China Seas, T. Ichiye ed., Elsevier, Amsterdam, pp. 399-408.

Lie, H.-J.,and S.-K. Byun, 1985. Summertime southward current along the east coast of Korea. Journal of the Oceanological Society of Korea 20, 22-27.

Lie, H.-J., S.-K. Byun, I. Bang, and C.,-H. Cho, 1995. Physical structure of eddies in the southwestern East Sea. Journal of the Korean Society of Oceanography 30, 170-183.

Lim, B., and K. Kim, 1995. A numerical study on the interaction of Ulleung Warm Eddy with topography and lateral boundary. Journal of the Oceanological Society of Korea 30, 565-583.

Matsuyama, M., Y. Kurita, T. Senjyu, Y. Koike, and T. Hayashi, 1990. The warm eddy observed east of Oki Islands in the Japan Sea (2). Umi to Sora 66, 67-75.

Miyao, T., 1994. The fractal dimension analysis applied to eddies in the Sea of Japan. Oceanographical Magazine 44, 13-30.

Nof, D., 1981. On the dynamics of equatorial outflows with application to Amazon's basin. Journal of Marine Research 39, 1-29.

Nof, D., and T. Pichevin, 1999. The establishment of the Tsugaru and the Alboran Gyres. Journal Physical Oceanography 29, 39-54.

Nof, D., and T. Pichevin, 2001. The ballooning outflows. Journal Physical Oceanography 31, 3045-3058.

Olson, D. B., 1991. Rings in the ocean. Annual Review of Earth and Planetary Sciences 19, 283-311.

Orlanski, I., 1976. A simple boundary condition for unbounded hyperbolic flows. Journal of Computational Physics 21, 251-269.

Ou, H. S., 2001. A model of buoyant throughflow: With application to branching of the Tsushima Current. Journal of Physical Oceanography 31, 115-126.

Parsons, A. T., 1969. A two-layer model for Gulf Stream separation. Journal of Fluid Mechanics 39, 511-528.

Perkins, H., W. J. Teague, G. A. Jacobs, K. I. Change, and M.-S. Suk, 2000. Currents in Korea-Tsushima Strait during summer 1999. Geophysical Research Letters 27, 3033-3036.

Preller, R., and P. Hogan, 1998. Oceanography of the Sea of Okhotsk and the Japan/East Sea coastal segment. In The Sea 11, ed. A. Robinson and K. Brink, John Willey and Sons, pp. 429-481.

Ramp, S. R., F. L. Bahr, C. J. Ashjian, and L. D. Talley, 2002. The Upper-Ocean Circulation in the Ulleung Basin During June-July 1999, submitted to Deep-Sea Research II.

Rostov, I., G. I. Yurasov, N. I. Rudyh, V. V. Moroz, E. V. Dmitreva, A. A. Nabiullin,F. F. Khrapchenkov and V. M. Bunim, 2001: Oceanographic Atlas of Bering Sea, Okhotsk Sea, and Japan/East Sea. CD-ROM, POI FEBRAS, Vladivostok, Russia.

Suda, K., and K. Hidaka, 1932: The results of the oceanographical observations on board R.M.S. Syunpu Maru in the southern part of the Sea of Japan in the summer of 1929, part I. J. Oceanogr. Imp. Mar. Observ. 3, 291-375 (in Japanese).

Sugimoto, T., and H, Tameishi, 1992. Warm-core rings, streamers and their role on the fishing ground formation around Japan. Deep-Sea Research I 39 (Suppl. S), S183-S201.

Tameishi, H., 1987. Applications of NOAA/AVHRR images to fisheries around Tsushima Strait. Fisheries Oceanography 51, 238-244.

Tanioka, K., 1968. On the East Korean Warm Current (Tosen Warm Current). Oceanographical Magazine 20, 31-38.

Toba, T., K. Tomizaqa, Y. Kurasawa, and K. Hanawa, 1982. Seasonal and year to year variability of the Tsushima-Tsugaru Currents system with its possible cause. La Mer 20, 41-51.

Uda, M., 1934. The results of simultaneous oceanographical investigations in the Japan Sea and its adjacent waters in May and June 1932. Journal of the Imperial Fisheries Experimental Station 5, 57-190 (in Japanese).

Veronis, G., 1973. Model of world ocean circulation: I. Wind driven, two-layer. Journal of Marine Research 31, 228-288.

Zalesak, S. T., 1979. Fully multidimensional flux-corrected transport algorithms for fluids. Journal of Computational Physics 31, 335-362.

Appendix

A List of Symbols and acronyms

f	Coriolis parameter $(f_0 + \beta y)$
g'	Reduced gravity, $g\Delta\rho/\rho$
h	Upper layer thickness
h_e	Eddy upper layer thickness
H	Undisturbed upper layer thickness
H_e	Upper layer thickness at the eddy center
L	Boundary current width (Figs. 4 and 10)
L_2	Width of square domain S (Fig. 4)
L_e	Basin zonal width (Fig.10)
Q	Boundary current transport
R	Eddy radius
R_1	Parameter defined as $8(g'H_e)^{1/2}/f_0$
R_d	Rossby radius of deformation, $(g'H)^{1/2}/f_0$
R_{de}	Rossby deformation radius of the eddy, $(g'H_e)^{1/2}/f_0$
S	Integration area bounded by $ABCD$ in Figs. 4 and 10
S^+, S^-	Subsets of S such that $y \geq 0$ and $y \leq 0$ respectively
u, v	Velocity components in Cartesian coordinates
$\bar{v}$	Current's mean speed
v_θ	Orbital velocity in the eddy
y_s, y_n	Latitudes of the southern and northern boundaries of S respectively (Figs. 4 and 10)
x_B	x-coordinate of point B in Fig. 10
β	Variation of the Coriolis parameter with latitude
ϵ	Small parameter equal to $\beta R_d/f_0$
ρ, $\Delta\rho$	Density and density difference between the layers
ν	Viscosity coefficient

κ	Coefficient of interfacial friction
ψ	Streamfunction (defined by $\psi_y = -uh$; $\psi_x = vh$)
ψ_∞	Limit of ψ as $x \to \infty$
$\widehat{\psi}$	$\psi - \psi_\infty$
ψ_e	Eddy stream function
τ^x	Zonal component of the wind stress
ADCP	Acoustic Doppler Current Profiler
EKWC	East Korea Warm Current
JES	Japan/East Sea
NKCC	North Korea Cold Current
TWC	Tsushima Warm Current
UWE	Ulleung Warm Eddy
WBC	Western Boundary Current

List of Tables

List of Figures

Experiment	Parameters	Resolution, Time Step	Basin size
E1	$f_0 = 0.8573 \times 10^{-4}$ s^{-1}, $\beta = 1.849 \times 10^{-11}$ m^{-1} s^{-1}, $g' = 0.014$ m^2 s^{-1}, $H = 300$ m, $\nu = 1500$ m^2 s^{-1}	15 km, 12 min	1500 km $\times$ 3000 km
E2	$f_0 = 0.8573 \times 10^{-4}$ s^{-1}, $\beta = 1.849 \times 10^{-11}$ m^{-1} s^{-1}, $g' = 0.014$ m^2 s^{-1}, $H = 300$ m, $\nu = 500$ m^2 s^{-1}	15 km 12 min	1500 km $\times$ 3000 km
E3	$f_0 = 0.8573 \times 10^{-4}$ s^{-1}, $\beta = 0$, $g' = 0.014$ m^2 s^{-1}, $H = 300$ m, $\nu = 500$ m^2 s^{-1}	15 km, 12 min	1500 km $\times$ 3000 km

Table 2
List of experiments

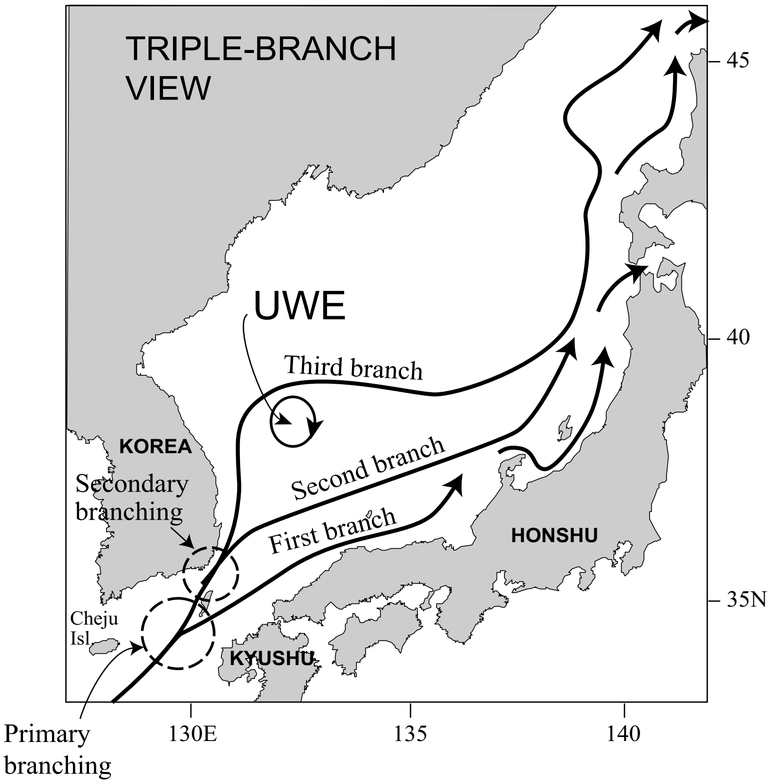

Fig. 1. Schematic diagram of the Tsushima Warm Current (TWC) and the triple branch view with the first branch, second branch, and third branch [sometimes referred to as the East Korean Warm Current (EKWC)]. The broken circles show the splitting of the TWC and the closed circle represents the Ulleung Warm Eddy (UWE). (Adapted from Preller and Hogan, 1998)

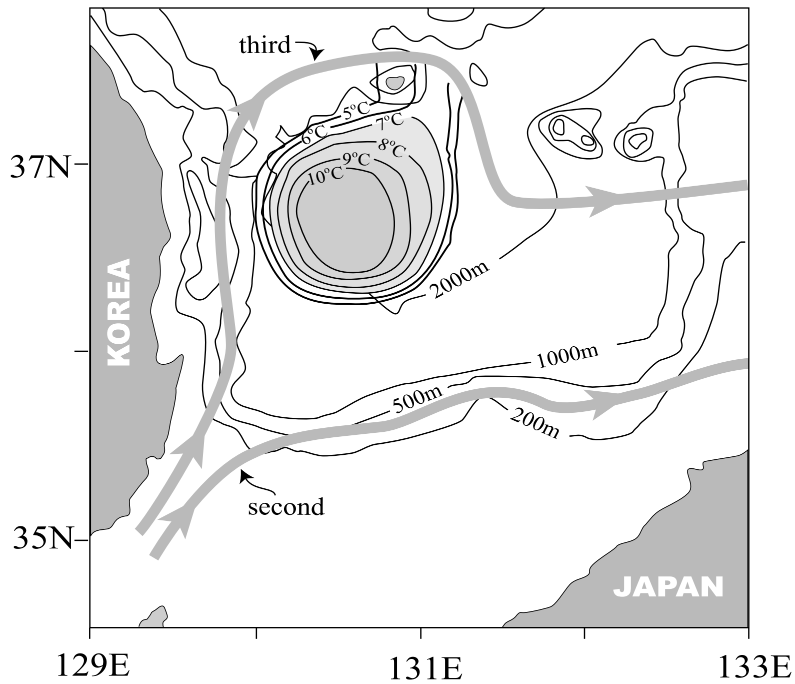

Fig. 2. Bathymetry and horizontal temperature distribution at 200 m depth during July 8-15, 1989, showing the Ulleung Warm Eddy (UWE). The temperature contour interval is 1°C. The arrowed lines show the third branch (EKWC) and the second branch. (Adapted from Lim and Kim, 1995)

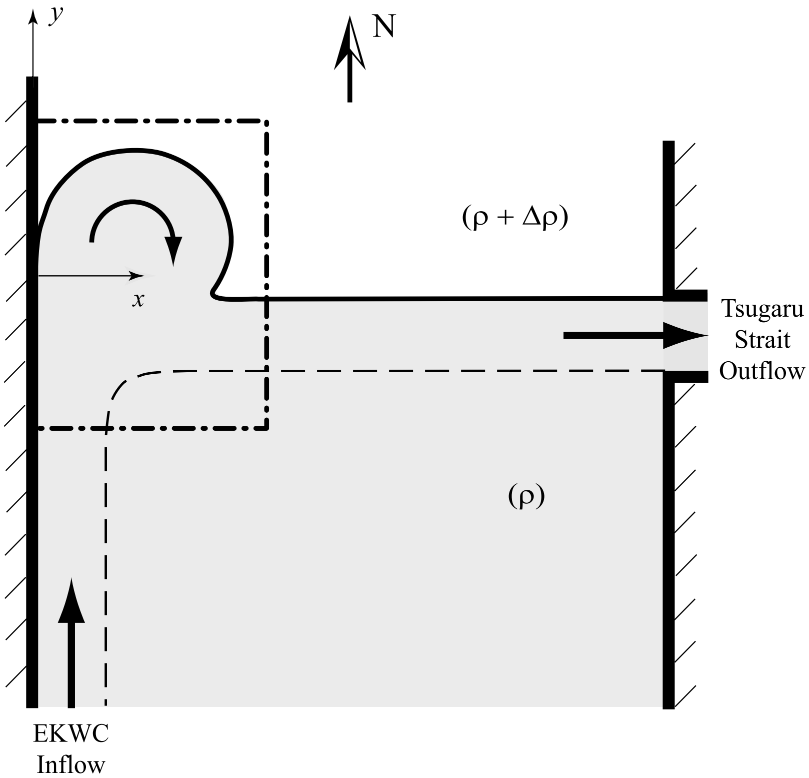

Fig. 3. Schematic diagram of the separation of the EKWC (defined as an inflow) forced by the Tsugaru outflow on the eastern side of the basin. The shaded area represents the region where the lighter layer is present. The origin of the coordinate system is situated at the separation point. A close up of the region bounded by the dashed-dotted line is shown in Fig. 4.

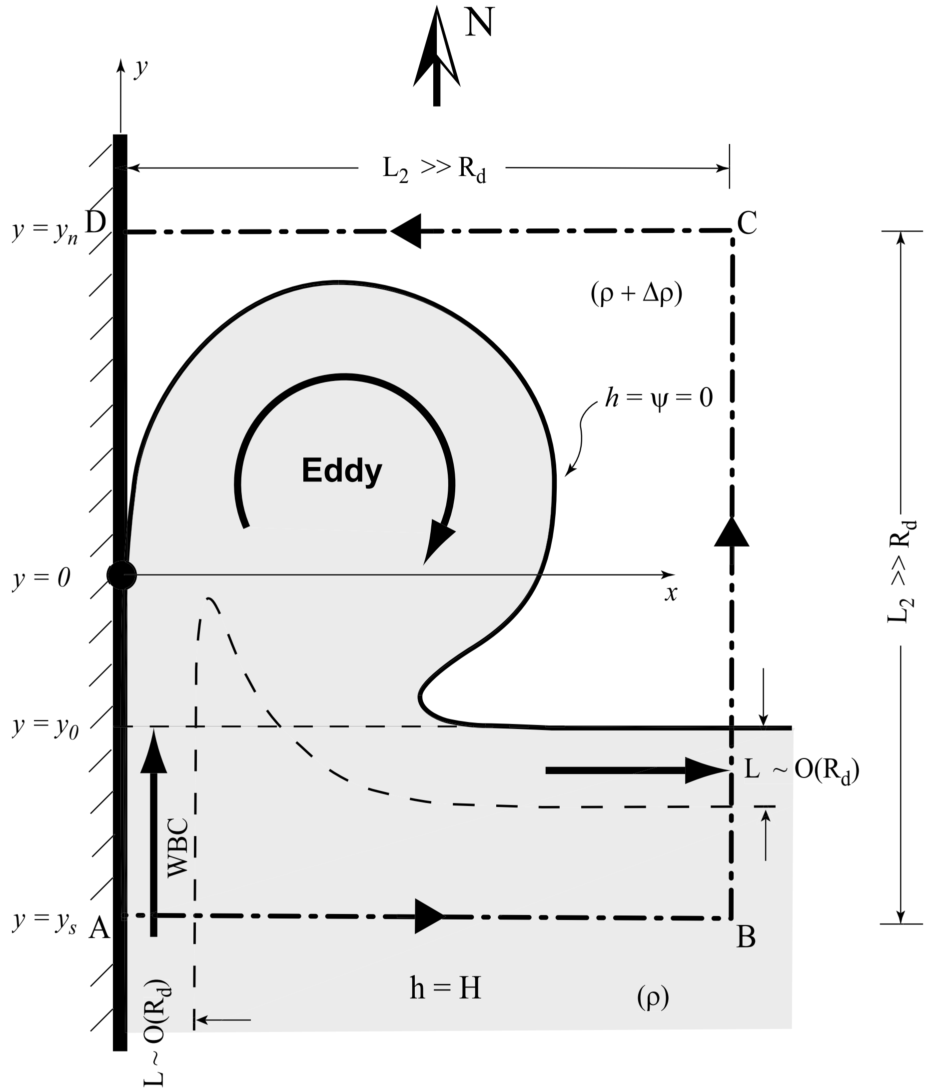

Fig. 4. A close up of the region bounded by the dashed-dotted line in Fig. 3. A northward flowing western boundary current (WBC) [with width of $O(R_d)$] in a layer of density ρ separates from the coast and forms an intrusion eddy. After the fluid circles within the eddy it flows zonally eastward. H is the undisturbed upper layer thickness at the basin interior. It will be shown that the eddy scale is of $O(R_d/\epsilon^{1/6})$ and that the momentum imparted on the region bounded by $ABCD$ through AB by the boundary current is balanced by the β-induced force of the anticyclonic eddy.

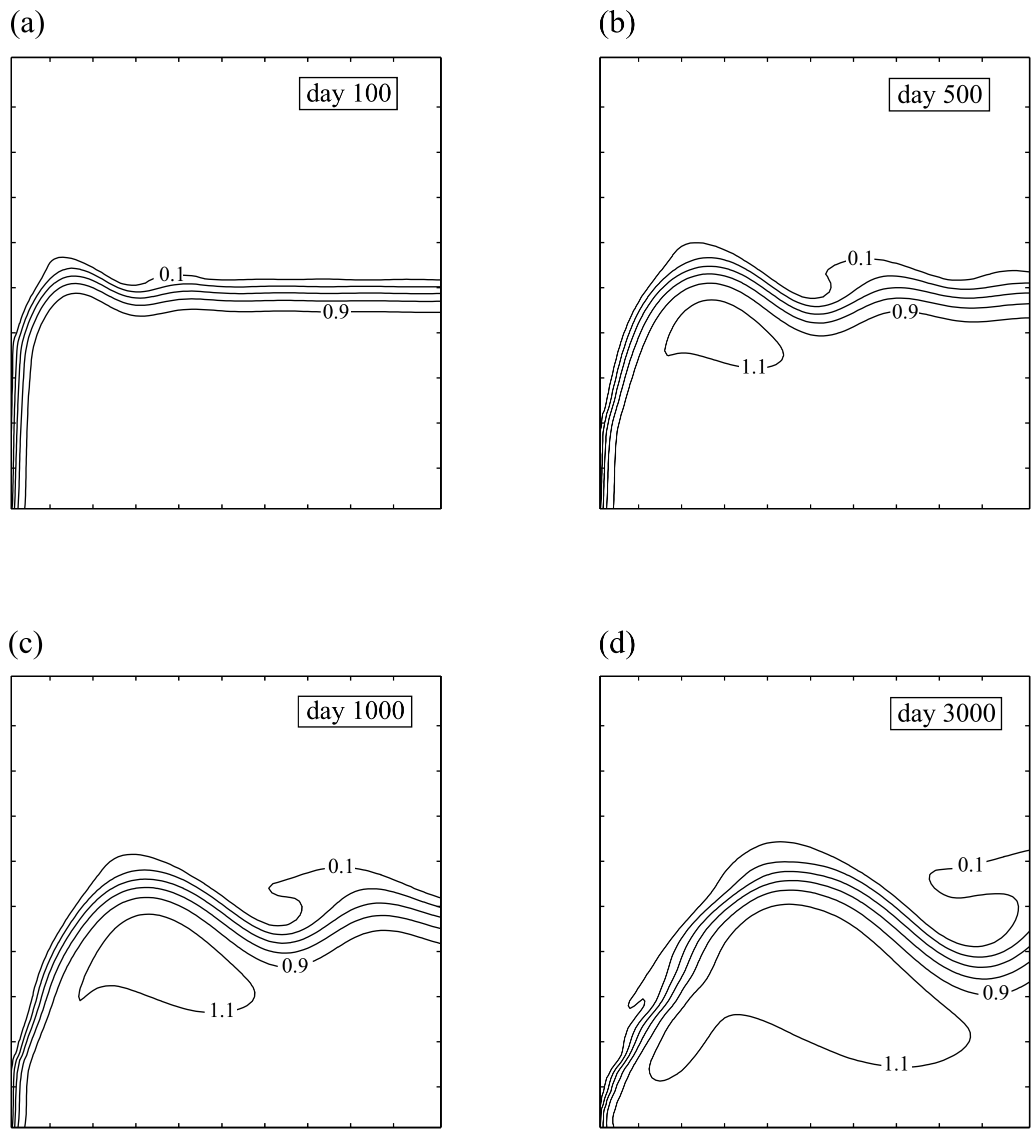

Fig. 5. Contour maps of the upper layer thickness nondimensionalized by $H = 300$ m for the f-plane run (experiment E3 in Table 1) at days: (a) 100; (b) 500; (c) 1000; (d) 3000. The contour spacing is 0.2. The axes marks are 10 grid points (150 km) apart.

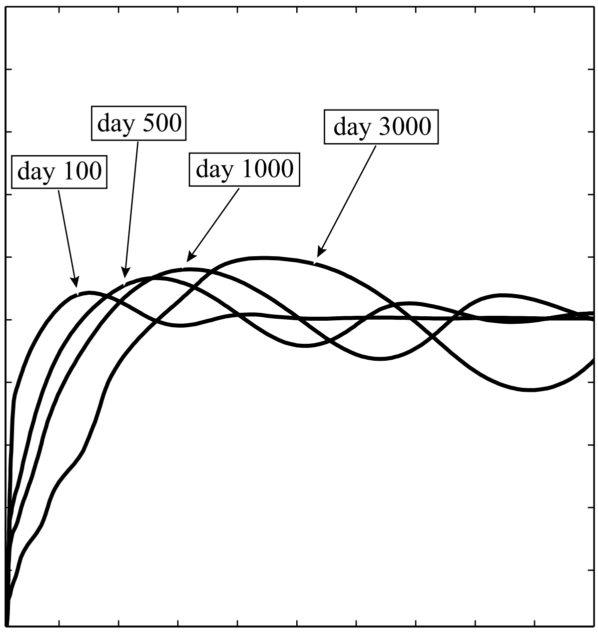

Fig. 6. Superposition of the 0.3 contours for the f-plane run (experiment E3 in Table 1) at day 100, 500, 1000, and 3000, showing the offshore movement of the system.

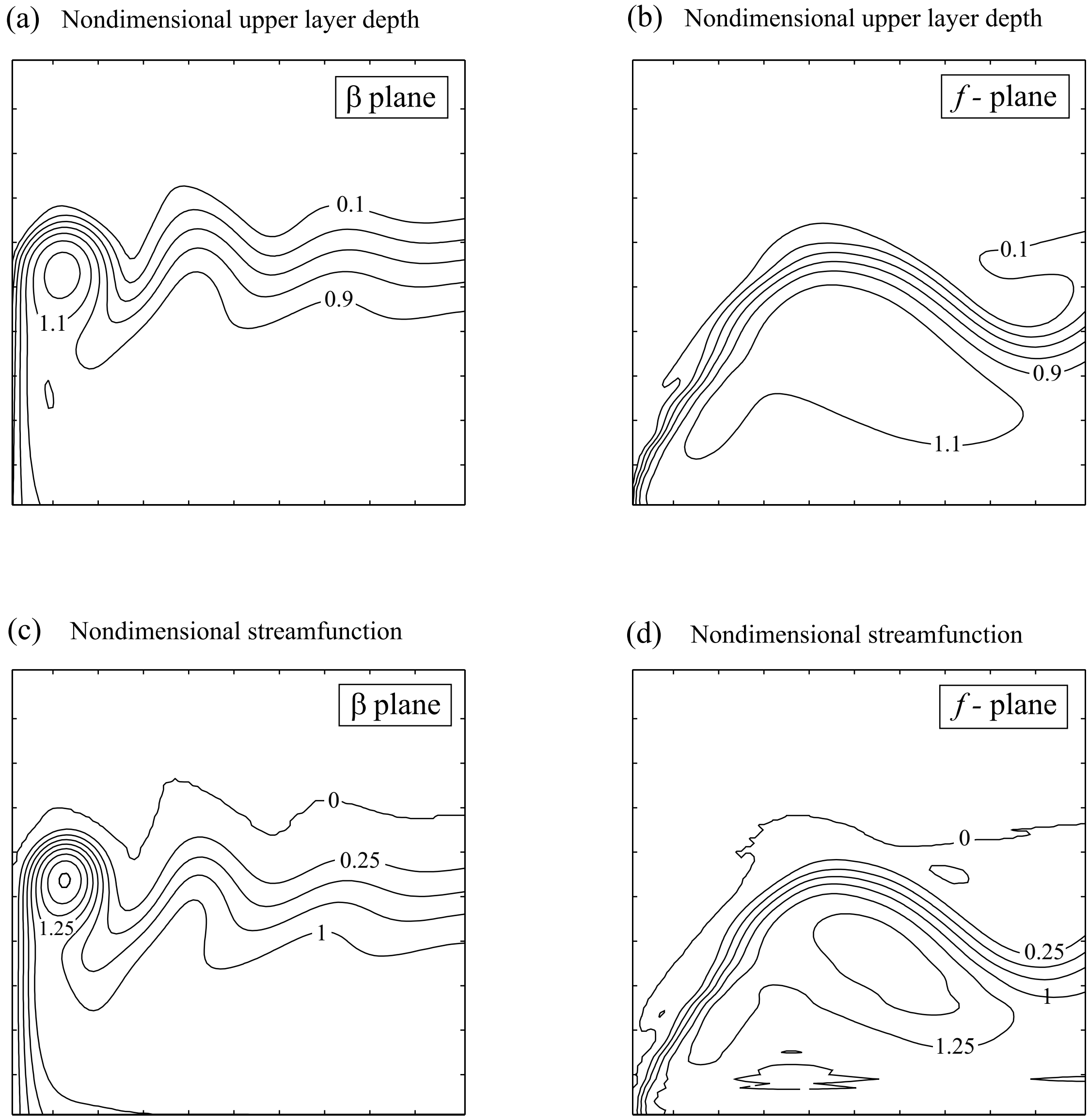

Fig. 7. Snapshots at day 3000: (a) Contour map of the nondimensional upper layer thickness (h/H) for the β-plane run (experiment E1 in Table 1). Contour spacing of 0.2; (b) Same as in (a) for the f-plane run (experiment E3 in Table 1); (c) Contour map of the nondimensional stream function $[\psi/(g'H/2f_0)]$ for the β-plane run (experiment E1 in Table 1). Contour spacing of 0.25; (d) Same as in (c) for the f-plane run (experiment E3 in Table 1). The axes marks are 10 grid points (150 km) apart.

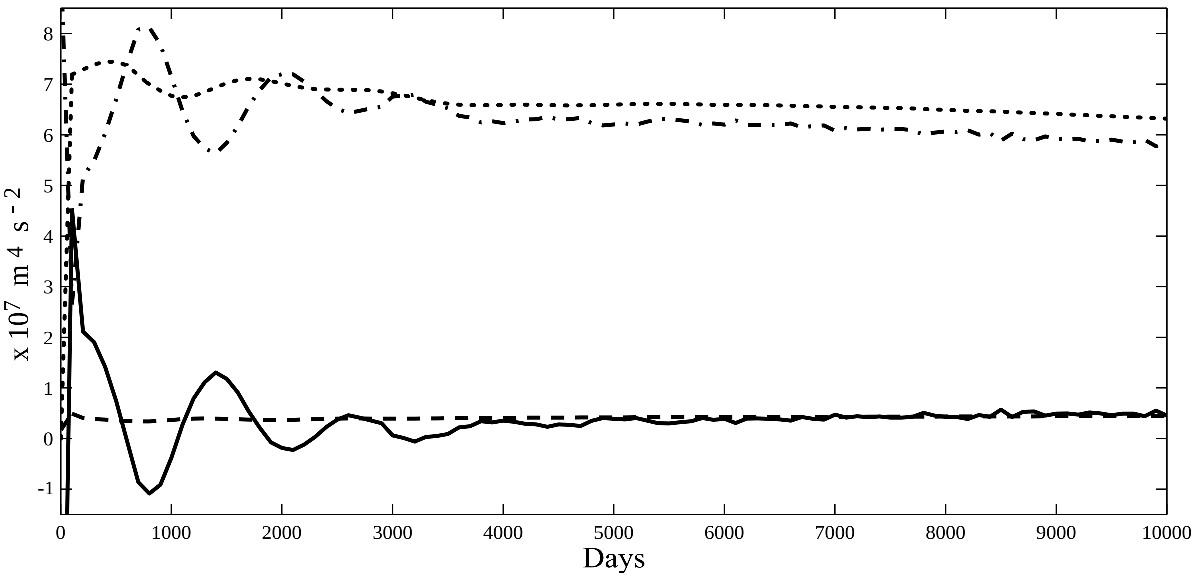

Fig. 8. Estimate of the terms in the equation (31) from the experiment E1 (Table 1): Dotted line: $\beta \iint_S \psi \, dx \, dy$; Dash-dotted line: $\frac{g'}{2} h^2(0, y_s) L_2$; Dashed line: $\int_0^L hv^2 \, dx$; Solid line: $\beta \iint_S \psi \, dx \, dy - \frac{g'}{2} h^2(0, y_s) L_2$.

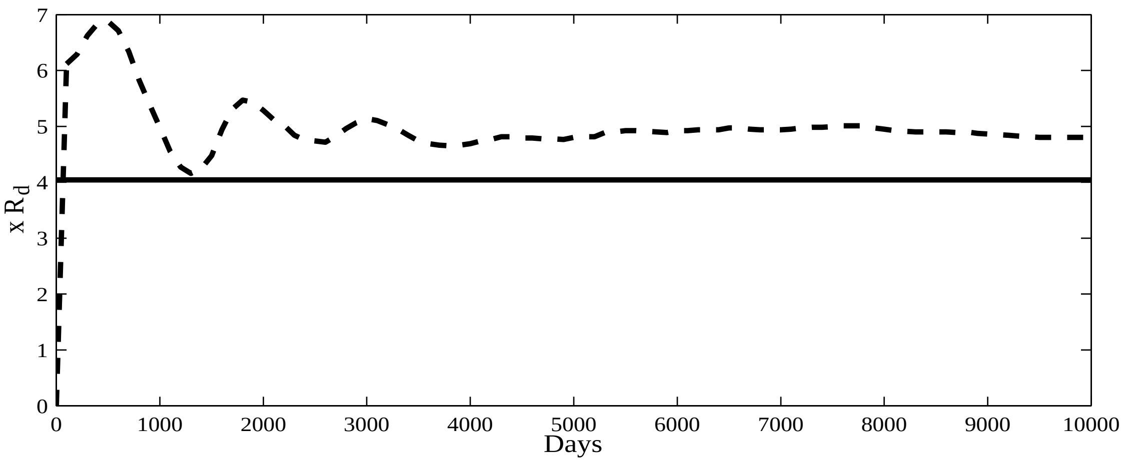

Fig. 9. Solid line: Analytical estimate of the eddy radius from equation (30). Dashed line: Numerical estimate (taking the value of 1.3 for the nondimensional streamline as the eddy boundary). Both plots are scaled by the Rossby radius.

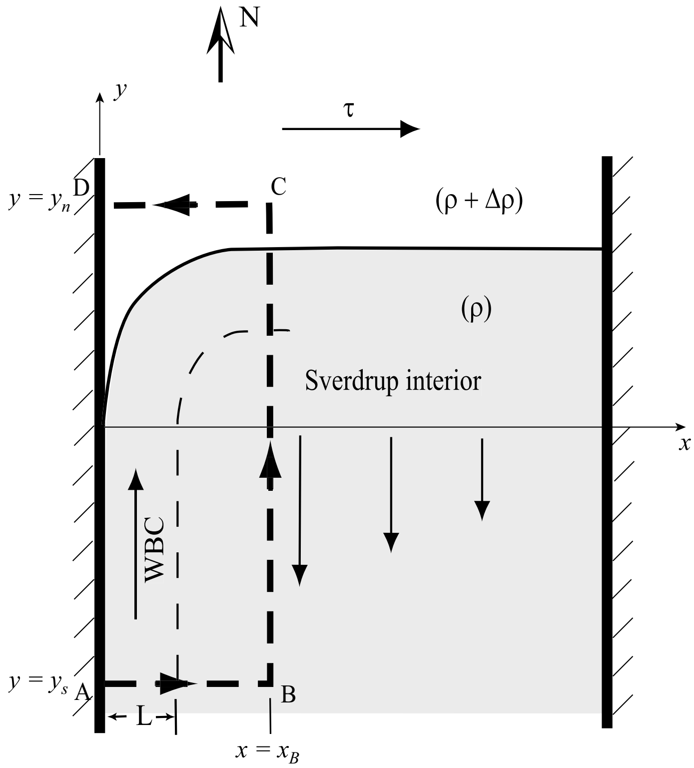

Fig. 10. Schematic representation of the linear limit, i.e., here we take the boundary current to be a linear frictional current rather than inertial. The shaded area represents the region where the lighter layer is present. The circulation is established by the wind stress τ; in the basin interior the slow southward Sverdrup flow takes place, while in the narrower western boundary layer (of width L) a stronger northward western boundary current (WBC) closes the anticyclonic gyre. In this linear limit the boundary current leaves the coast by vanishing the upper layer thickness (á là Parsons, 1969).